INTERNATIONAL JOURNAL FOR NUMERICAL METHODS IN FLUIDS
Int. J. Numer. Meth. Fluids 2009; **61**:658–682
Published online 22 December 2008 in Wiley InterScience (www.interscience.wiley.com). DOI: 10.1002/fld.1979

Flow past a transversely oscillating square cylinder in free stream at low Reynolds numbers

A. P. Singh, A. K. De*,†, V. K. Carpenter, V. Eswaran and K. Muralidhar

Department of Mechanical Engineering, Indian Institute of Technology Kanpur, Kanpur 208 016, India

SUMMARY

This paper reports simulation results for free-stream flow past an oscillating square cylinder at $Re = 100$ and 150, for oscillating-to-natural-shedding frequency ratios of $0.5 \leqslant f_r \leqslant 3.0$ at a fixed oscillation amplitude of 0.2 of the cylinder width. The transformed governing equations are solved in a non-inertial frame of reference using the finite volume technique. The 'lock-in' phenomena, where the vortex shedding becomes one with the oscillation frequency, is observed near the natural shedding frequency ($f_r \approx 1$). Beyond the synchronization band, downstream recovery of the wake to its stationary (natural) state (frequency) is observed in cross-stream velocity spectra. At higher forcing frequencies, a phase lag between the immediate and the far wake results in a shear layer having multi-polar vortices. A 'Vortex-switch' accompanied by a change in the direction of energy transfer is identified at the 'lock-in' boundaries. The variation of aerodynamic forces is noticed to be different in the lock-in regime. The velocity phase portrait in the far wake revealed a chaotic state of flow at higher excitation though a single (natural) frequency appears in the spectra. Copyright © 2008 John Wiley & Sons, Ltd.

Received 1 September 2007; Revised 5 November 2008; Accepted 9 November 2008

KEY WORDS: oscillating square cylinder; lock-in; vortex shedding; vortex switch; energy transfer; vorticity

1. INTRODUCTION

For last few decades, engineers concerned with the design of bridges, buildings and offshore structures have paid much attention to fluid–structure interactions. The vortex dynamics behind a bluff body, causing fluctuating forces acting on the body, has been a topic of research with many groups. As the induced vibration of a structure forms an important issue for its stability, much of the literature deals with the cause, nature and the consequences of what is known as 'flow-induced vibration'. Highly informative reviews for flow around a (CC) have been written by Williamson [1]

*Correspondence to: A. K. De, Department of Mechanical Engineering, Indian Institute of Technology Kanpur, Kanpur 208 016, India.
†E-mail: arkde@iitk.ac.in

and Zdravkovich [2]. A common approach to study fluid–structure interactions is to force the body to oscillate with a predefined motion that approximates the flow- or vortex-induced motion. In this type of study [3–11], flow features are examined as the body is subject to a forced oscillation.

When a bluff body is set in a transverse oscillation, near its natural frequency, i.e. when the forced oscillation frequency is close to the natural shedding one, the wake behind the body attaches to it and oscillates with a single frequency. The band of frequencies where this synchronization is seen to occur is known as the 'lock-on' [3, 7, 10, 11] regime. The boundaries of this band, its bandwidth and the characteristic features associated with it offer interesting fluid mechanical aspects. Ongoren and Rockwell [3] performed a hydrogen bubble visualization experiment on cylinders of various cross sections subject to controlled oscillations at Reynolds numbers in the range of 584–1300. The study noted that near the boundaries of this band, the structure of shedding vortices flip from one side of the cylinder to the other at a particular position of the cylinder. This feature has been known as the 'vortex switch' [10]. Bishop and Hassan [4] found distinct changes in both the amplitude and timing of vortex-induced forces exerted on the cylinder as the oscillation frequency is changed within the primary lock-in range. Along with the evidence of hysteresis, they also observed phase jump in the lock-in range where an almost 180° shift in the phase between the lift coefficient and the cylinder motion occurs. Stansby [5], through his experiments, associated jumps in the phase angle with changes in the wake width from being greater than that of the cylinder below the critical excitation frequency, from which lock-in starts, to being less than that for the cylinder above the critical excitation frequency. Several insightful attempts have been made to identify the resonance and 'lock-on' range [6, 7], timing of vortex formation [8] and the layout of wake structure [9]. Blackburn and Henderson [10] observed phase switching at oscillation frequencies near the natural shedding frequency of the fixed cylinder, which they attributed to changes in the direction of mechanical energy transfer between the cylinder and wake. Guilmineau and Queutey [11] explained the mechanism of vortex switching from either side of the cylinder, i.e. development of high vorticity concentration in the near wake of the cylinder.

While a number of literature contributions addressed the laminar unsteady flow over a stationary square cylinder for a range of Reynolds numbers and dealt with a number of issues, no comprehensive study exists for flow past an oscillating square cylinder in the low and moderate Reynolds numbers ($Re<500$) range. To the best of our knowledge, the issues that have made the problem of oscillating CC interesting have not been tested extensively on the square cylinder in the low Reynolds number range. Yang *et al.* [12] studied flow structures in the wake for different oscillation speeds and frequencies with amplitude of oscillation kept at $1/\pi$ for flow over a rectangular cylinder placed in a channel at $Re=500$. Bearman and Obasaju [13] found the amplification of the coefficient of fluctuating lift to be much less than that of a CC at high Reynolds numbers, $5.8\times10^3\leqslant Re\leqslant3.2\times10^4$. They also reported a different variation of phase angle between the lift and the cylinder displacement compared to the oscillating CC case. Taylor and Vezza [14] used a discrete vortex method to simulate flow past a transversely oscillating square cylinder. At $Re=20\,000$, they predicted the 'lock-in' phenomena around the resonance point ($f_r=1$) and explained various states of the flow field above and below this regime.

The primary aim of the present work is to examine the flow past a transversely oscillating square cylinder in the laminar regime for a range of frequencies (around the natural shedding frequency) and at a low (compared with the length of the cylinder) amplitude of oscillation. We intend to determine the synchronization band, the nature of vortex shedding within and outside this range, behavior of the force coefficients and oscillation of the near and the far wake in relation to the

DOI: 10.1002/fld

forced oscillation, thereby categorizing the flow regimes. We also intend to examine the 'vortex switch' at the 'lock-in' boundaries and its relation with the mechanical energy transfer.

1.1. Problem description

The objective of the present work is to numerically study the flow features caused by harmonic and non-harmonic oscillations of a square cylinder placed in free stream. The cylinder oscillates in the transverse direction with a fixed amplitude of 0.2 of the cylinder width at a range of frequencies, $0.5 \leqslant f_r \leqslant 3.0$, where f_r is the ratio of the cylinder excitation frequency (f_e) to the natural vortex shedding frequency (f_0) of the stationary cylinder. The vortex shedding mechanism, phase shift in the vortex layout, energy transfer and the behavior of the aerodynamic forces in conjunction with fluid–body interaction have been studied. A schematic description of the flow in the inertial frame of reference is shown in Figure 1(a). Dimensions of the domain considered for simulations are $X_u = 8$, $X_d = 24$, $H = 18$ and $d = 1$. The Reynolds number ($Re = \frac{U_{in} d}{\nu}$), based on cylinder width and inflow velocity, are 100 and 150.

The organization of the paper is as follows. We first present the governing equations and boundary conditions followed by the numerical details. In the subsequent sections simulation results are

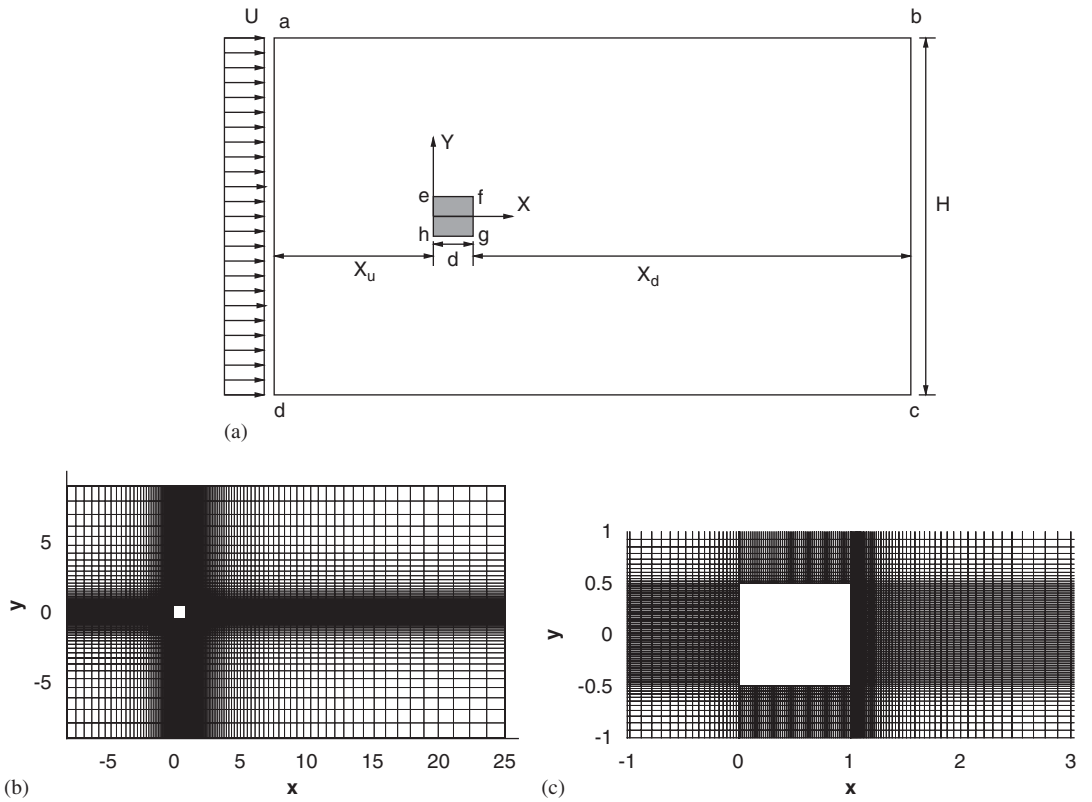

Figure 1. (a) Schematic of the flow domain; computational grid; (b) full view; and (c) zoomed in near the cylinder.

DOI: 10.1002/fld

presented for a number of issues, such as synchronization, wake recovery, vortex switch, flow states, aerodynamic force coefficients and mechanical energy transfer. Finally, we conclude the main findings of the work in Section 5.

2. MATHEMATICAL MODELING

Free-stream flow past a transversely oscillating cylinder can be simulated in a non-inertial frame [15] attached to the cylinder without changing the position of the artificial far-stream boundaries [9–11]. In this approach, the effect of the non-inertial frame is represented by a simple source term in the transverse momentum equation, facilitating computational convenience by avoiding the re-meshing of the whole domain that is required if a fixed inertial frame were instead used.

2.1. Governing equations

The normalized mass and momentum conservation equations for incompressible, laminar flows in the inertial laboratory frame of reference are given by

$$\frac{\partial u_i}{\partial x_i}=0 \tag{1}$$

$$\frac{\partial u_i}{\partial t}+\frac{\partial (u_j u_i)}{\partial x_j}=-\frac{\partial p}{\partial x_i}+\frac{1}{Re}\frac{\partial^2 u_i}{\partial x_j \partial x_j} \tag{2}$$

where $u_i(u, v)$ and $x_i(x, y)$ correspond to the velocity and coordinate direction in the inertial frame of reference, respectively. The transformation rule between the non-inertial frame of reference fixed to the oscillating cylinder and the inertial laboratory frame is

$$x_i=\bar{x}_i+X_i, \quad u_i=\bar{u}_i+U_i \tag{3}$$

where the barred quantities are in the non-inertial frame. The origin position $X_i(X, Y)$ and velocity components $U_i(U, V)$ of the non-inertial frame with respect to the laboratory frame are given by

$$X=0, \quad Y=A_c \sin \omega t, \quad U=0, \quad V=A_c \omega \cos \omega t \quad \text{with } \omega=2\pi f_r St$$

where A_c, f_r and St are the amplitude of oscillation, frequency ratio and Strouhal number or vortex shedding frequency of the stationary cylinder at the same Reynolds number, respectively. The above governing equations are written in the non-inertial frame of reference as

$$\frac{\partial \overline{u_i}}{\partial \overline{x_i}}=0 \tag{4}$$

$$\frac{\partial \bar{u}_i}{\partial t}+\frac{\partial (\bar{u}_j \bar{u}_i)}{\partial \bar{x}_j}=-\frac{\partial p}{\partial \bar{x}_i}+\frac{1}{Re}\frac{\partial^2 \bar{u}_i}{\partial \bar{x}_j \bar{x}_j}-A_i \tag{5}$$

where $A_x=\mathrm{d}U/\mathrm{d}t=0$, $A_y=\mathrm{d}V/\mathrm{d}t=-A_c\omega^2 \sin \omega t$ represents the instantaneous acceleration of the non-inertial frame, i.e. the cylinder.

DOI: 10.1002/fld

2.2. Boundary conditions

The relevant boundary conditions in both reference frames are discussed below:

Inlet: At the inlet, $v=0$ condition changes to $\bar{v}=-V$, while $u/U_{\text{in}}=1$ does not change ($\bar{u}=1$) as the cylinder moves only in the cross-stream direction. The pressure assumes the Neumann condition, $\partial p/\partial x=0$.

Far stream: At the far-stream longitudinal boundaries, the free slip condition ($\partial u/\partial y=0, v=0$) is employed. The normal component of velocity, v changes its value from zero in the inertial frame to $-V$ in the non-inertial frame while the condition for the longitudinal velocity component and the pressure remains the same, $\partial u/\partial y=\partial\bar{u}/\partial\bar{y}=\partial p/\partial y=0$.

Outlet: At the outlet, the Orlanski boundary condition [16], $\partial u_i/\partial t+u_c\partial u_i/\partial x=0$ ($u_i=u, v$), which facilitates the undistorted passage of vortices across the exit plane, is the same for both the frames. At this boundary pressure is specified, $p=0$.

Cylinder surface: The no-slip conditions on the cylinder surface, $u=0$ and $v=V$, become $\bar{u}=\bar{v}=0$ in the non-inertial frame of reference. Normal pressure gradient is set to zero at all the cylinder faces, $\partial p/\partial n=0$.

3. NUMERICAL DETAILS

3.1. Finite volume formulation and solution algorithm

Computations are carried out by a finite-volume-based numerical code using a collocated or non-staggered arrangement of variables. Time integration of the governing equations are carried out by the implicit Crank–Nicolson scheme, which is theoretically second-order accurate (leading-order truncation error is $O(\Delta t^2)$). The governing equations are solved by a two-step projection method. In the first step, a provisional velocity field is computed excluding the pressure and mass flux taken as the latest available one

$$\frac{u^*_{iP}-u^n_{iP}}{\Delta t}V_P+\frac{1}{2}\left(\sum_f F^{n+1,l}_f u^*_{if}+\sum_f F^n_f u^n_{if}\right)=\frac{1}{2Re}\left(\sum_f F^*_{dfi}+\sum_f F^n_{dfi}\right)-A_i V_P \tag{6}$$

where P and f denote the center and faces of the computational cells with volume V_P while the index $i=1,2$ correspond to stream-wise (x) and cross-stream (y) directions, respectively. The face velocities are then calculated by adding a pressure gradient term with the linearly interpolated face values from the provisional velocities

$$u_f=Ł(u^*_P, u^*_{\text{nb}})-\frac{\Delta t}{\rho}(\nabla p)_f \tag{7}$$

where Ł denotes linear interpolation of the provisional velocities between the cell center (P) and its neighboring points (nb). This yields mass flux at the cell faces as

$$F_f=F^*_f-\Delta t(\nabla p)_f\cdot\mathbf{S}_f \tag{8}$$

The finite volume approximation of the integrated continuity equation is given by

$$\sum_f F^{n+1}_f=0 \tag{9}$$

DOI: 10.1002/fld

When the mass flux calculated from Equation (8) is inserted in the flux balance equation (Equation (9)), the following equation for the pressure is obtained:

$$\sum_f F_f^{n+1,l+1} = \sum_f F_f^* - \Delta t \sum_f (\nabla p)_f \cdot \mathbf{S}_f = 0 \implies \sum_f (\nabla p).\mathbf{S}_f = \frac{1}{\Delta t} \sum_f F_f^* \tag{10}$$

Equation (10) is equivalent to the Poisson equation for pressure correction in SIMPLE-like algorithms. The converged pressure of Equation (10) is used for new estimate of mass flux in Equation (8). Here l denotes the flux loop counter that is iterated until flux converges. The converged mass flux along with the pressure that estimates it corresponds to the divergence free velocity field. These quantities are then used to solve for the velocities u^{n+1} and v^{n+1} using the momentum equations integrated over a finite volume

$$\frac{u_{iP}^{n+1} - u_{iP}^n}{\Delta t} V_P + \frac{1}{2} \left(\sum_f F_f^{n+1} u_{if}^{n+1} + \sum_f F_f^n u_{if}^n \right)$$

$$= -\sum_f p_f^{n+1} S_{fi} + \frac{1}{2Re} \left(\sum_f F_{dfi}^{n+1} + \sum_f F_{dfi}^n \right) - A_i V_P \tag{11}$$

The sequential steps that constitute the solution method is written below.

1. Initialize the variables and start with mass flux, $F_f^{n+1,l} = F_f^n$.
2. Solve Equation (6) for u^* and v^*.
3. Compute F_f^* required for the pressure equation.
4. Solve the pressure equation, Equation (10).
5. Estimate new mass flux from Equation (8) and set $l = l+1$.
6. Repeat steps 2–5 till convergence of the fluxes, $|F_f^{n+1,l+1} - F_f^{n+1,l}| < \varepsilon$ is achieved.
7. Solve Equation (11) for u^{n+1} and v^{n+1} using converged fluxes and pressure.
8. Set $n = n+1$ and repeat all the steps (2–7) for the next time step.

Interpolations of variables at the cell center or at the cell faces are achieved by the second-order scheme. It should be noted that the theoretical accuracy of the spatial interpolation scheme is based on the uniform grid framework, and application of it in non-uniform mesh leads to a reduction of accuracy depending upon the nature and intensity of the non-uniformity [17]. All systems of simultaneous linear equations arising from Equations (6), (10) and (11) are solved by the Gauss–Seidel successive over-relaxation technique. The convergence is assessed after each iteration and the solution residual (in the root mean square (RMS) sense) is brought below 10^{-5} for Equations (6), (10) and (11) while 10^{-6} for the flux convergence. The grid used in the present work has been 192×120 with refinement done near the cylinder. A uniform grid of 60×60 is used on the cylinder surface. The nearest grid lines in the x- and y-directions from the cylinder are 0.007 and 0.02, respectively. Figure 1(b) shows a typical grid while Figure 1(c) shows a detailed view near the cylinder. In all the calculations the time increment $\Delta t = 0.01$ is used. Owing to the fully-implicit nature of the algorithm, no numerical instabilities are observed in any of the cases studied here. The solution of the stationary cylinder provides the initial condition for the oscillating case at the same Reynolds number.

DOI: 10.1002/fld

To reduce the computational time, the code has been parallelized using message passing interface. By decomposing the computational domain into a number of subdomains, calculations are distributed among different processors keeping the load balancing factor (ratio of maximum to minimum number of cells across all the subdomains) as close as possible to unity. It has been observed that with increase in the communication time compared with the computational time, the parallel algorithm provides lesser speed-up (ratio of times taken in a single processor to multi processor environment). Thus, the code is parallelized keeping communication among processors as minimum as possible. A higher-order interpolation that uses a stencil size more than two requires extra communication at the interfaces of the subdomains. Hence, we have chosen the interpolation scheme as the second-order technique that uses three points in the computational stencil.

3.2. Refinement test

The numerical results are sensitive to the number of grid points chosen in the computations. More accurate results require finer mesh, which increases the cost of computations. To check the effects of mesh size, the two-dimensional stationary square cylinder problem has been tested for three different grids. The results obtained for $Re=100$ and 150 are compared for all the three cases. The comparisons are shown in Table I where N_S indicates the number of grid points taken on each face of the cylinder. At $Re=100$, the results show a change of 0.67, 2 and 0.6% in $\overline{C_D}$, St and C_{Lrms}, respectively, between the finest and the coarsest grids. This change becomes 2.29, 1.92 and 2.5% at $Re=150$. Since the comparisons show a maximum change in results less than 3% over all the three grids, we have chosen 192×120 grid for all subsequent calculations considering the cost-effectiveness of the computations.

3.3. Code validation

The numerical code is tested for Stokes' first and second problems involving a moving boundary and a few already reported cases for stationary square cylinder. While the first two problems test the formulation for the non-inertial reference frame, the third case compares results with the published literature for the unsteady bluff body flow. Figures 2(a) and (b) show comparison with analytical results for the Stokes' problems while Figures 2(c) and (d) compare the present results with that from the literature [18–20] for the stationary cylinder case.

3.4. Domain-dependence test

In flows with unsteady wake, selection of the downstream length is important as it affects the quality of the solution. Too small a length distorts the convecting vortices that form the Kármán

Table I. Computational features of the refinement test at $Re=100$ and 150.

Re	Grid size	N_S	$\overline{C_D}$	St	C_{Lrms}
100	192×120	60	1.51	0.147	0.16
	202×130	70	1.51	0.15	0.16
	250×150	80	1.52	0.15	0.161
150	192×120	60	1.482	0.156	0.28
	202×130	70	1.502	0.157	0.283
	250×150	80	1.516	0.159	0.287

DOI: 10.1002/fld

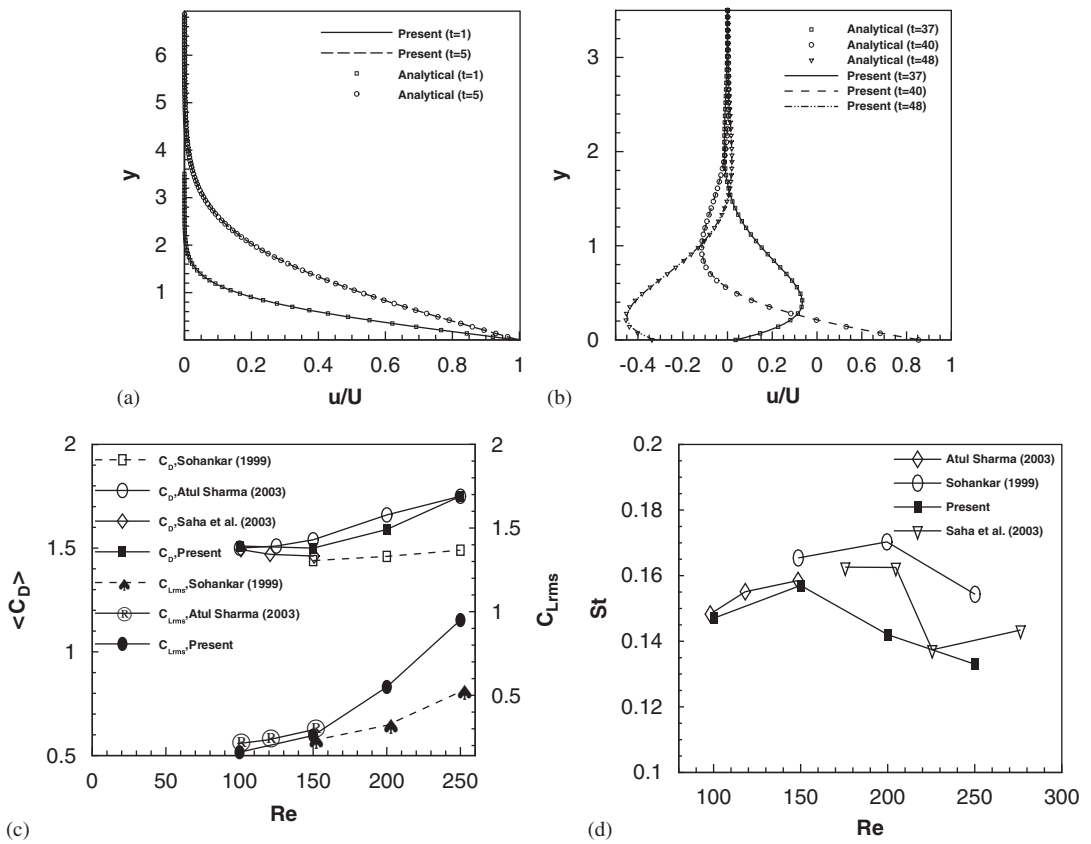

Figure 2. Comparative results: Stokes' (a) first and (b) second problem; flow past a stationary square cylinder: (c) $\langle C_D \rangle$–Re and (d) St–Re.

vortex street. However, choice of a larger length requires more grid points that leads to increase in computational time. Thus, selection of the downstream length is crucial. Sohankar *et al.* [21] reported that the Neumann boundary condition works well compared with the Orlanski condition for flow past a square cylinder at incidence. However, for large downstream length ($X_\mathrm{d}=26$), differences in results and flow pattern do not appear for the two boundary conditions. In an earlier study [22], we noticed that when the downstream length is smaller ($X_\mathrm{d}=15$), integral parameters vary considerably. However, at a larger length ($X_\mathrm{d}=25$), changes in X_d leads to differences in integral parameters less than 2%. Also, increasing the downstream length demands more grid points to maintain a consistent grid spacing near the cylinder and away from it. Based on these observations, we have chosen $X_\mathrm{d}=24$ for all the calculations reported in this paper.

For unconfined flows, a larger domain size (smaller blockage) in the cross-stream direction indicates larger incoming flow, which changes the solution. However, changes in the results are trivial at smaller blockage ratios. For instance, Sohankar *et al.* [21] reported that if the blockage is reduced from 5 ($H=20$) to 2.5% ($H=40$), the maximum change in $\overline{C_D}$, St and C_Lrms is 1.4%. They observed a higher change ($\approx 7\%$) in the base suction coefficient. We have tested

DOI: 10.1002/fld

Table II. Details of the domain dependence test at $Re=100$.

Blockage (%)	Grid size	$\overline{C_D}$	St	C_{Lrms}
10 ($H=10$)	192×120	1.605	0.154	0.171
5 ($H=20$)	192×180	1.51	0.147	0.16
2 ($H=50$)	192×240	1.504	0.148	0.162

the effects of domain size in the cross-stream direction at $Re=100$. The results are compiled in Table II. In these simulations, the number of grid points in the x-direction is fixed with maximum and minimum grid lengths set at $\Delta_x=0.75$ and $\delta_x=0.007$, respectively. For different blockage ratios in the cross-stream direction, the minimum ($\delta_y=0.02$) and the maximum ($\Delta_y=0.35$) grid sizes are retained by varying the number of grid points. When the blockage ratio is changed from 10 to 5%, changes in $\overline{C_D}$, St and C_{Lrms} are 6.29, 4.76 and 6.87%, respectively. However, as the blockage is further reduced to 2%, these changes become 0.4, 0.68 and 1.25%. Thus, considering the cost of computations due to large number of grid points for $H>20$ and the changes in the results, we have chosen $H=18$ for all the calculations to be followed.

4. RESULTS AND DISCUSSION

In addition to the pressure, the surface tangential component of the cylinder acceleration plays an important role in the vortex formation and shedding mechanism when the cylinder is in motion. Blackburn and Henderson [10] reported a similar observation in the case of a CC. There are two modes of vortex shedding observed in the simulations. In the first mode, vortices form and are shed from the two rear-end corners, the same process as that of a stationary cylinder. The second mode involves growth of vortices on the two horizontal surfaces of the cylinder, where they subsequently merge with the shear layers to be shed into the wake. Both modes have been observed to coexist and, depending upon the cylinder acceleration either of them may dominate over the other.

4.1. Wake synchronization

Figure 3 shows the shedding frequency (f_{s}) over a range of excitation frequencies (f_{e}) at $Re=100$ and 150, respectively. In the graph, the ordinate shows the vortex shedding frequency (f_{s}) normalized by the excitation frequency ($f_{\mathrm{e}}/f_{\mathrm{s}}$) to ascertain the synchronization band ($f_{\mathrm{s}}=f_{\mathrm{e}}$) while the abscissa shows the frequency ratio ($f_{\mathrm{r}}=f_{\mathrm{e}}/f_0$). A band limited wake-synchronization, similar to the case of a CC [4, 8, 10, 23], is observed (regions 'bc' and '$\mathrm{b_1c_1}$') in the figure. This region is known as the 'lock-in' regime where the vortex shedding occurs at exactly the excitation frequency, i.e. the shedding synchronizes with the excitation. The synchronization bands are found to be $0.95\leqslant f_{\mathrm{r}}\leqslant1.2$ at $Re=100$ and $0.8\leqslant f_{\mathrm{r}}\leqslant1.3$ at $Re=150$. The bandwidths are smaller than what Tanida *et al.* [7] found in their experiment with the CC at a comparable Reynolds number ($Re=80$). In the figures, the excitation frequencies below the 'lock-in' range (point 'a') correspond to a sub-harmonic excitation and frequencies above the 'lock-in' range (points 'd' and 'e') represent super-harmonic states.

DOI: 10.1002/fld

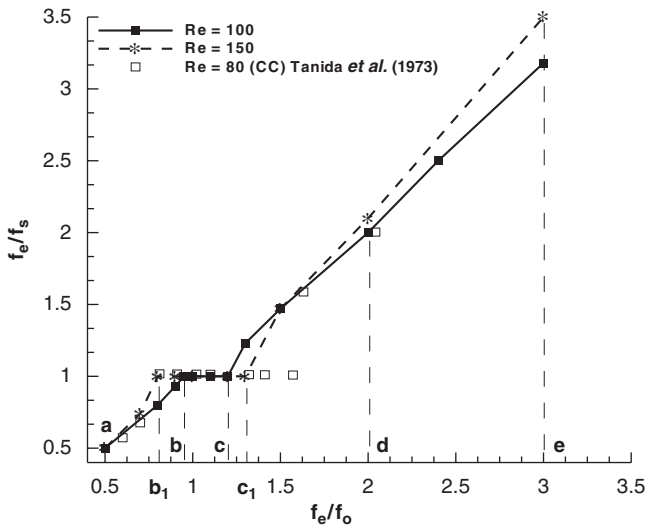

Figure 3. Vortex shedding frequency over the excitation frequency showing 'lock-in' region.

4.1.1. Near-wake shedding frequency. To estimate the dominant frequencies in the near-wake flow, the spectra of force coefficients are obtained using Discrete Fourier Transformation [15] of the signals recorded during the simulations. The sampling rate for the signals of force coefficients and the velocity components is $\alpha_S = 100$ (in non-dimensional unit). According to the Nyquist–Shannon sampling theorem, the upper bound for frequency component of the signal that can be reconstructed from the recorded discrete data is $\alpha_B < \alpha_S/2 = 50$. The maximum dominant frequency (≈ 0.5) resolved by the samples is considerably smaller than this limit. The step size between two discrete frequencies is approximately $\delta f = 0.0025$ in all the plots.

Figures 4 and 5 show a few selected drag and lift spectra at different excitation frequencies for $Re = 100$ and 150, respectively. Outside the 'lock-in' range, the lift spectrum shows peaks at both the shedding and excitation frequencies indicating co-existence of both the natural and the forced mode of oscillation. But in the drag spectrum, peaks occur not only at the shedding and body frequencies, but also at harmonics and combinations (sum and difference) of them as evident in Figures 4(a), (d) and 5(a), (d). In the synchronized regime, occurrence of a single peak confirms the wake being locked to the cylinder and it oscillates with the cylinder. Note that the peak frequency for the drag coefficient is twice that of the peak frequency for the lift coefficient.

4.1.2. Far-wake shedding frequency. The far-wake oscillation frequency is calculated from the spectra of the cross-stream velocity (v) recorded at a distance of five units downstream of the cylinder's rear face along the center line of the cylinder ($y = 0$). Figures 6 and 7 show a few selected v-spectra and the phase portrait between the u and v velocities at both harmonic and non-harmonic excitation frequencies. Below the 'lock-in' frequencies, the appearance of only the natural frequency (see Figure 6(I)(a)) implies that cylinder excitation does not affect the natural oscillation mode of the far wake. In the synchronized regime the peak occurs at the frequency that is the same as the excitation frequency, as is evident from Figures 6(II)(a) and 7(I)(a). In this range,

DOI: 10.1002/fld

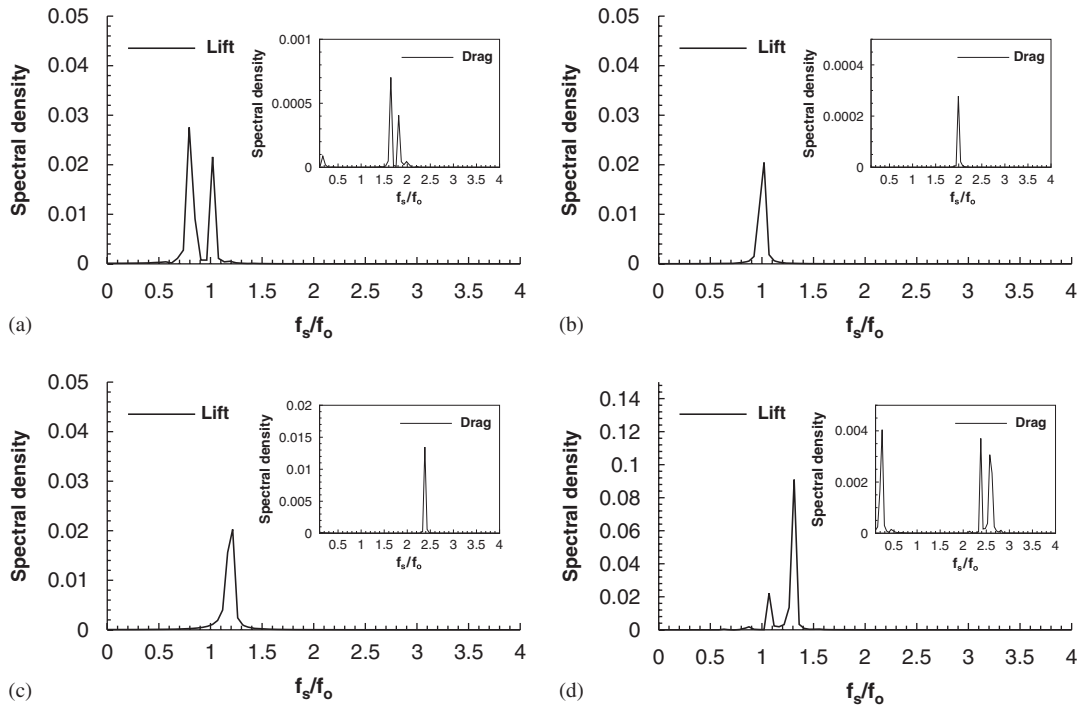

Figure 4. Drag (inset) and lift spectra at $Re=100$: (a) $f_r=0.8$; (b) $f_r=1.0$; (c) $f_r=1.2$; and (d) $f_r=1.3$.

a single-orbit phase portrait (Figures 6(II)(b) and 7(I)(b)) further confirms the existence of a single frequency. Thus in the 'lock-in' regime, the entire wake attaches with the cylinder to oscillate at the excitation frequency of the cylinder. As f_e goes beyond the 'lock-in regime', the far wake again recovers its natural frequency and the natural mode of oscillation dominates over the forced one, which can be seen in Figures 6(III)(a) and 7(III)(a). However, a quasi-periodic phase diagram at $Re=100$ (Figure 6(III)(b)) changes to a chaotic nature at $Re=150$ (Figures 7(II), (III)(b)). This points out a possible onset of instabilities at lower super-harmonics at $Re=150$. A partial recovery of the far wake with the existence of multiple peaks in the v-spectrum can be seen in Figure 7(II)(a) at a non-harmonic excitation showing the presence of frequencies intermediate to the excitation and the natural shedding frequencies.

4.2. Vortex shedding mechanism

Sequences of vortex shedding at a non-harmonic ($f_r=0.8$ at $Re=100$) excitation are shown in Figures 8(I)(a)–(e), where vortex shedding occurs at the natural frequency. The cylinder oscillation and the vortex shedding are out of phase, as evident from Figures 8(I)(a) and (e), which are qualitatively different. Owing to the low Reynolds number and the forced frequency, the shape of the shear layers and their fluttering motion is close to the stationary case. An increase in the Reynolds number results in thinning and stretching of the shear layers with more intense fluttering. Note, for a sub-harmonic excitation at $f_r=0.5$ ($Re=150$), shown in Figures 8(II)(a)–(e), asynchronous shedding is apparently in phase with the cylinder oscillation. As the excitation frequency is half

DOI: 10.1002/fld

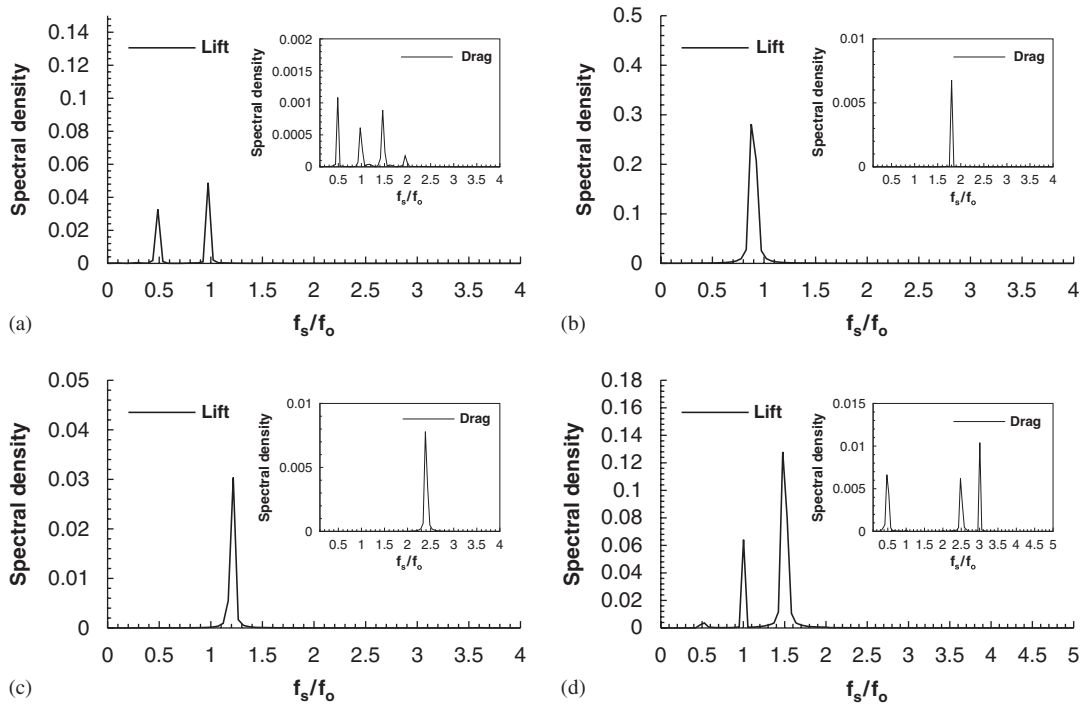

Figure 5. Drag (inset) and lift spectra at $Re = 150$: (a) $f_r = 0.5$; (b) $f_r = 0.9$; (c) $f_r = 1.2$; and (d) $f_r = 1.5$.

the natural frequency, two pairs of vortices are observed to shed, and the state of the wake is identically the same as the cylinder completes a full cycle ((a) and (e) correspond to $y = -Y_{max}$).

In the synchronized period, vortex shedding takes place at the excitation frequency of the cylinder and the whole wake oscillates with the same frequency. This fact is further verified by the in-phase shedding of a single pair of vortices in the wake, shown in Figures 9(a)–(i) with (a) and (i) being identical for the case $f_r = 1.2$ at $Re = 150$. Increase in the acceleration of the cylinder results in a disorganized near-wake structure. Note that vortices, as they travel downstream in the wake remain on the same side of the longitudinal center line where they were shed.

At frequency ratios above the 'lock-in' regime, formation of vortices from the top and bottom surfaces of the cylinder becomes apparent (see Figure 10). This mode of vortex formation is synchronized with the cylinder oscillation. This second ('forced') mode of vortex generation dominates over the first ('natural') one as cylinder oscillation increases beyond the 'lock-in' period. The far wake, however, recovers the natural frequency mode above the synchronous period. Thus, vortices forming from the horizontal surfaces of the cylinder coalesce, leading to the existence of multi-polar vortices attached to the cylinder. Figures 10(a) and (b) demonstrate the bi-polar and tri-polar nature of the vortices in the near wake for $f_r = 2$ and $f_r = 3$, respectively. The figures also show that shedding of vortices in the far-wake occurs at the natural frequency. The same recovery process in the wake was also reported by Ongoren and Rockwell [3].

For all the cases studied, $0.5 \leqslant f_r \leqslant 3$, $Re = 100, 150$, the 2S mode of vortex topology is found in the wake. For non-harmonic cases, vortex shedding and the cylinder oscillation are out of phase

DOI: 10.1002/fld

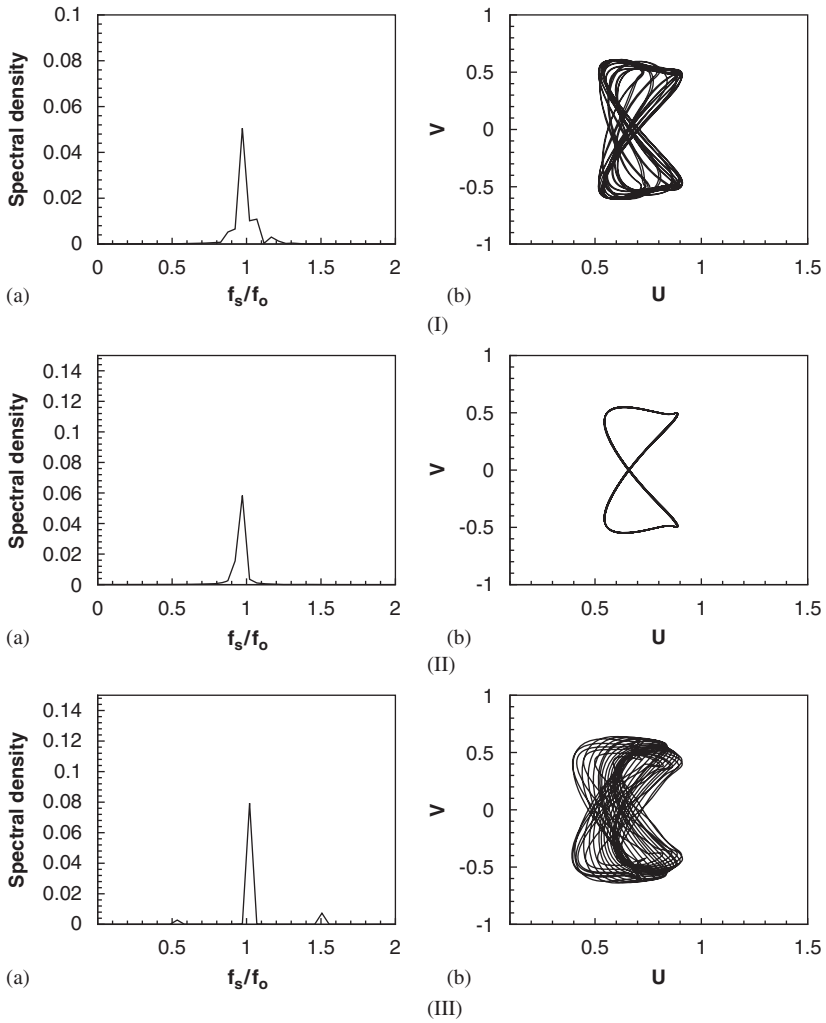

Figure 6. (a) v velocity spectra in the far wake and (b) phase portrait between u and v velocities at $Re=100$ for (I) $f_r=0.9$; (II) $f_r=0.95$; and (III) $f_r=1.5$.

and thus a cylinder oscillation cycle does not correspond to exactly one pair of shed vortices. On the other hand, for harmonic cases, though the cylinder induces its oscillation to the near wake, the far wake recovers the natural shedding mode. This results in the formation of multi-polar vortices.

The topology of the vortices in the wake is known to be important since it sheds lights on the possible explanation of the wake transition in accordance with its behavior at different Reynolds number. Moreover, the experiments of Ongoren and Rockwell [3] showed that the formation of vortices (timing) and their shedding into the wake differ dramatically as the shape of the bluff object changes. In the present study, at both Reynolds numbers, the '2S' mode of wake type is found near the frequency ratio one ($f_r \approx 1$). However, a closer look at the wake snapshots

DOI: 10.1002/fld

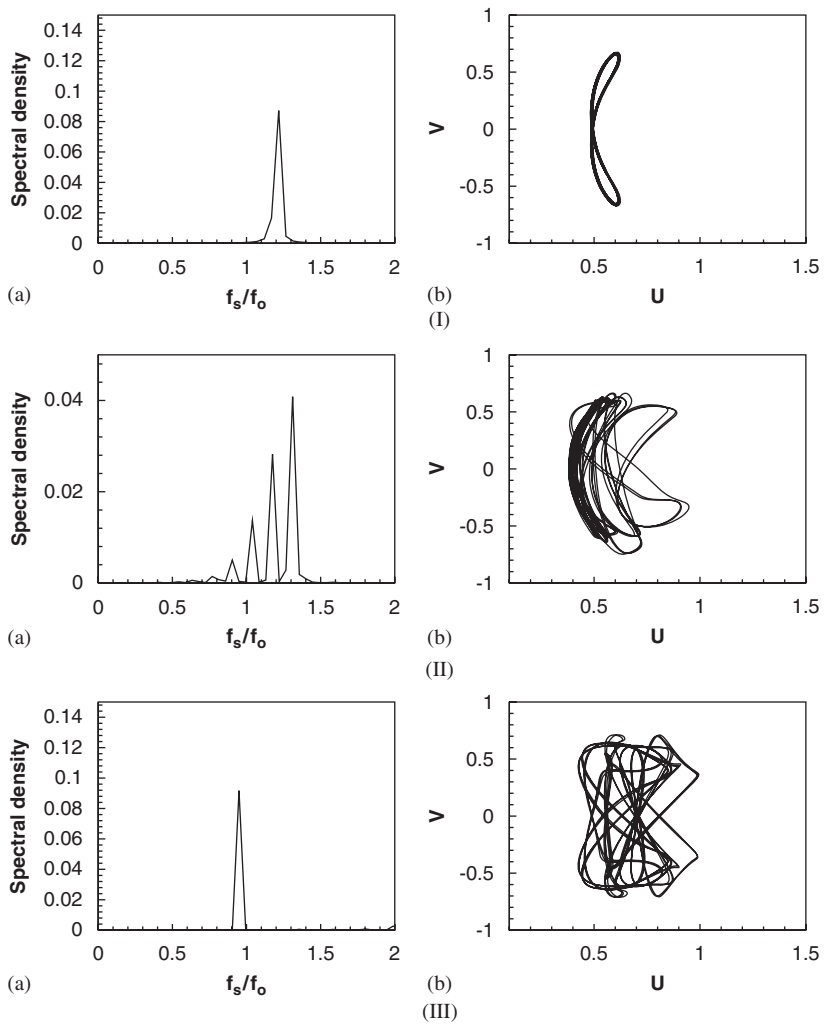

Figure 7. (a) v velocity spectra in the far wake and (b) phase portrait between u and v velocities at $Re = 150$ for (I) $f_r = 1.2$; (II) $f_r = 1.3$; and (III) $f_r = 2$.

(Figures 8–10) suggests that this mode is closer to what Williamson and Roshko [24] classified as 'C(2S)' mode where smaller vortices coalesce into larger structures in the near-wake region. The rotational aspect of these vortices reveals a similarity of this mode with that of the 'Antisymmetrical mode A-III' of Ongoren and Rockwell [25]. It should be noted that all the previous literature studies that analyzed the mode of the wake dealt with moderate to high Reynolds number. Thus, only a qualitative comparison should be made as the flow features are expected to be different at this range of Reynolds numbers compared with the low Reynolds number laminar flows. We have not observed the 'P+S' mode in any of the cases computed here. At higher frequency ratio, pairing of the vortices are observed and as the cylinder oscillation is considerably higher than the

DOI: 10.1002/fld

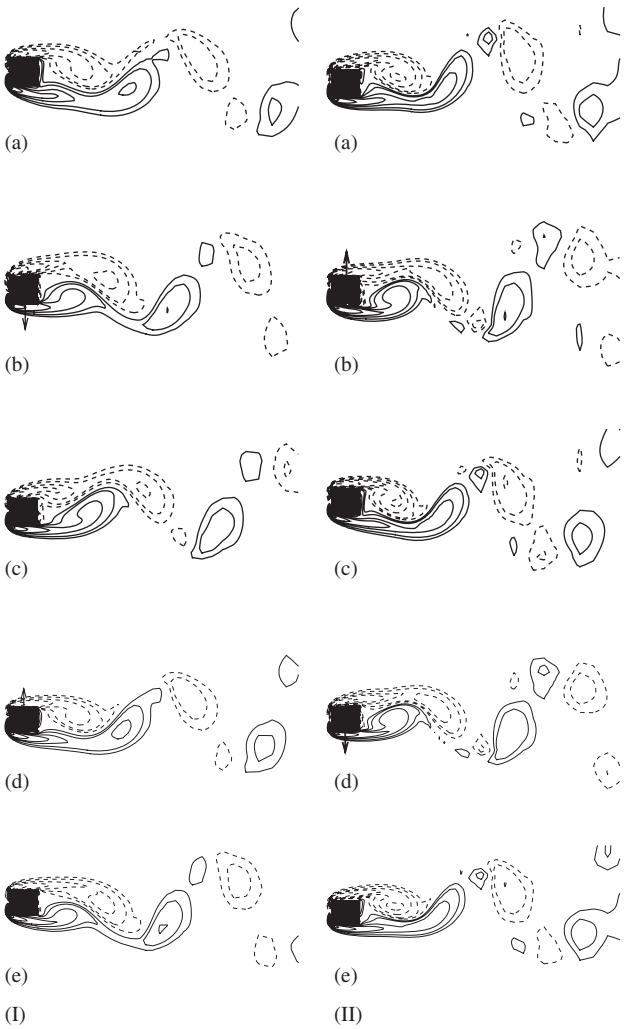

Figure 8. Instantaneous vorticity contours (dashed for negative values) for a cycle of cylinder oscillation. Arrows indicate the direction of the cylinder movement: (a) $y=Y_{\max}$; (b) $y=0$; (c) $y=-Y_{\max}$; (d) $y=0$; and (e) $y=Y_{\max}$ for (I) $f_r=0.8$, $Re=100$. (a) $y=-Y_{\max}$; (b) $y=0$; (c) $y=Y_{\max}$; (d) $y=0$; and (e) $y=-Y_{\max}$ for (II) $f_r=0.5$, $Re=150$.

wake, a single vortex is shed into the wake for one oscillation cycle of the cylinder i.e. the 'S' mode is evident.

4.3. Vortex switch

Figures 11(a)–(i) show instantaneous vorticity fields at $Re=150$ in the near-wake region for different excitation frequencies when the cylinder is at $y=-0.7Y_{\max}$ and moving upwards. In Figure 11(b) (at $f_r=0.7$), shedding takes place from the top rear corner shear layer (shown in dashed as negative vorticity) while for the same cylinder position in Figure 11(c) (at $f_r=0.8$), it is

DOI: 10.1002/fld

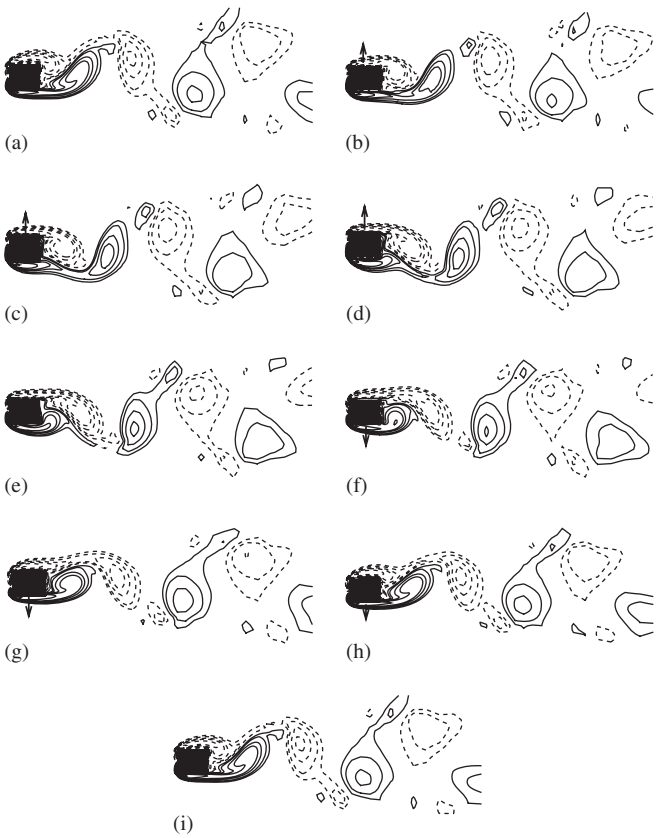

Figure 9. Instantaneous vorticity contours (dashed for negative values) at eight equi-spaced phases of cylinder oscillation for $f_r = 1.2$, $Re = 150$. Arrows indicate the direction of the cylinder movement: (a) $y = -Y_{max}$; (b) $y = -0.7Y_{max}$; (c) $y = 0$; (d) $y = 0.7Y_{max}$; (e) $y = Y_{max}$; (f) $y = 0.7Y_{max}$; (g) $y = 0$; (h) $y = -0.7Y_{max}$; and (i) $y = -Y_{max}$.

the bottom rear corner shear layer (shown in solid as positive vorticity) that is shedding a vortex into the near wake. Clearly, at the boundary of the 'lock-in' regime, the topology of vortex shedding from the corners of the cylinder switches sides. This is known as 'vortex switching' and has been previously reported [4, 5, 10] for the CC case. A similar reverse switch is observed at the upper boundary of the 'lock-in' regime between $f_r = 1.2$ and $f_r = 1.3$ (see Figures 11(f) and (g)). As the excitation frequency increases above the 'lock-in' regime, the length of the shear layers reduces and the shed vortices shrink owing to higher acceleration of the cylinder, which counteracts the free development of the attached shear layers and their separation. Signs of multi-polar vortices (see Figure 11(i)) can also be observed at harmonics ($f_r = 2$) above the synchronization period.

4.4. Flow regimes

The spectra and the phase portraits (see Figures 6 and 7) between u and v velocities, obtained from the far-wake signals described in Section 4.1.2, reveal the state of the flow with increase in Reynolds number and the excitation frequency. Below the synchronization period, while the

DOI: 10.1002/fld

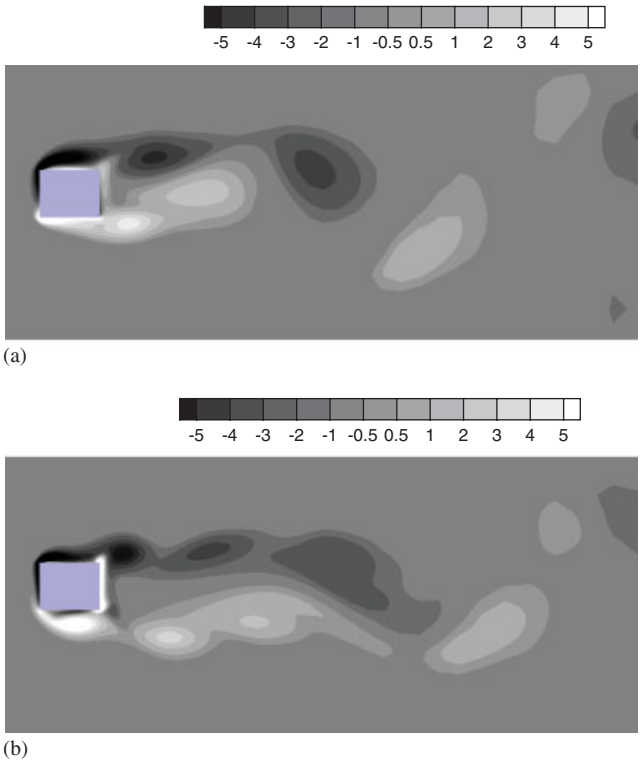

Figure 10. Vorticity contours at an instant for super-harmonic excitations at $Re=100$ showing multi-polar vortices: (a) $f_r=2.0$, $Re=100$ and (b) $f_r=3.0$, $Re=100$.

cylinder moves with the forced frequency, the wake retains its natural frequency. Both modes show up as peaks in the spectrum, though with comparatively different amplitude, a quasi-periodic state is evident from Figure 6(I)(b). In the 'lock-in' regime, as the whole wake attaches to the cylinder and oscillates with it, a single peak is obtained accompanied by a phase plot indicating a perfectly periodic state, shown in Figures 6(II)(b) and 7(I)(b). The effect of Reynolds number becomes evident above the 'lock-in' range. At $Re=150$, the wake shows transition from a low-chaotic state (Figure 7(II)(b)) at $f_r=1.3$ to a highly chaotic state (Figure 7(III)(b)) at $f_r=3$. However, a number of limit cycles almost parallel to each other (Figure 6(III)(b)) are found at $Re=100$ implying the quasi-periodic nature of the wake even at $f_r=1.5$. Thus, below the 'lock-in' regime, the wake is quasi-periodic in nature that becomes perfectly periodic near the natural frequency of the stationary cylinder ($f_r=f_e/f_0\approx 1$). Beyond the synchronization band, though the far wake recovers the natural shedding frequency, signs of instabilities show up with the increase in f_r, becoming prominent at higher Reynolds number.

4.5. Force coefficients

The time traces of drag and lift coefficients, shown in Figures 12 and 13, indicate the occurrence of twin frequencies in the non-synchronization regime, though not with a prominent pattern much

DOI: 10.1002/fld

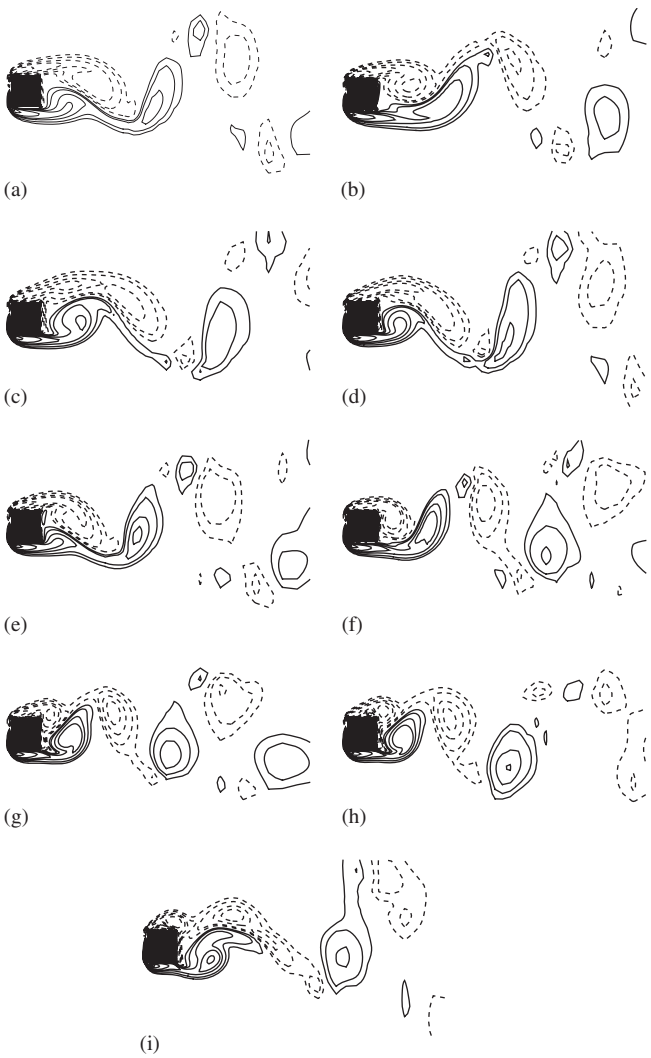

Figure 11. Instantaneous vorticity contours (dashed for negative values) when the cylinder is at $y=-0.7Y_{\max}$ for different f_r at $Re=150$: (a) $f_e/f_o=0.5$; (b) $f_e/f_o=0.7$; (c) $f_e/f_o=0.8$; (d) $f_e/f_o=0.9$; (e) $f_e/f_o=1.0$; (f) $f_e/f_o=1.2$; (g) $f_e/f_o=1.3$; (h) $f_e/f_o=1.5$; and (i) $f_e/f_o=2.0$.

below the synchronization period (see Figure 13(a)). A beat pattern comprising two wave forms—the natural mode of oscillation and the imposed oscillation by the cylinder, is observed below (at $f_r=0.9$ for $Re=100$) and above ($f_r=1.3$ for $Re=150$) the 'lock-in' regime. In the synchronized regime, a single frequency signal with a nearly constant amplitude ($f_r=0.95$ for $Re=100$ and $f_r=0.8, 1.2$ for $Re=150$) confirms that the wake oscillates with the cylinder at the forced frequency. However, at very large excitation frequencies, time signals of the force coefficients essentially show a transition from the weakly twin-frequency mode ($f_r=2$ for $Re=100$) to the single-frequency

DOI: 10.1002/fld

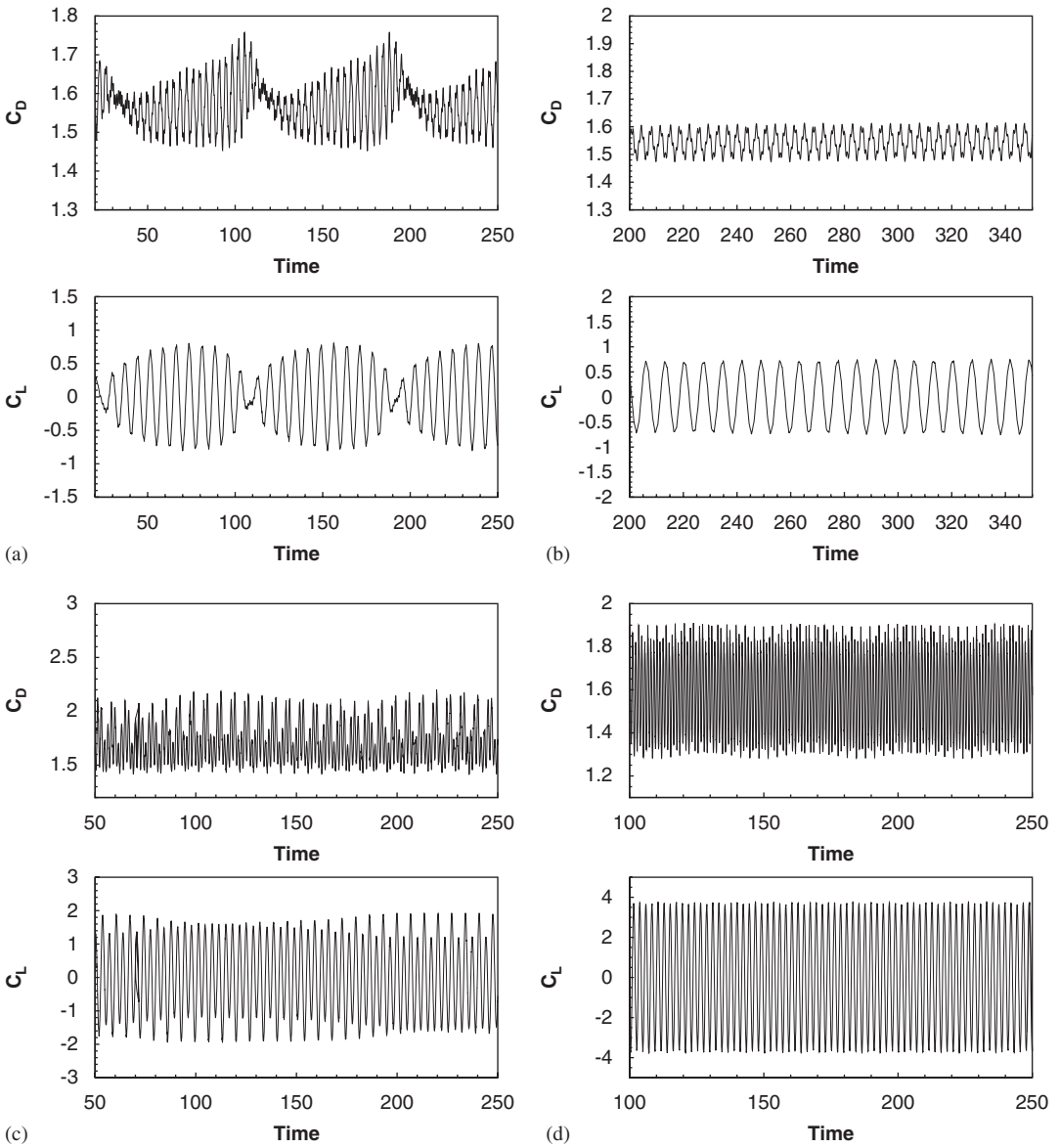

Figure 12. Time traces of drag and lift coefficients at $Re=100$: (a) $f_r=0.9$; (b) $f_r=0.95$; (c) $f_r=2.0$; and (d) $f_r=3.0$.

mode ($f_r=3$ for $Re=100$)—the forcing or the excitation frequency, even while the far wake is dominated by the natural frequency.

The variation of the mean and RMS of the force coefficients with the excitation frequency are shown in Figures 14(a)–(c) along with results of a few low Reynolds number CC cases for the sake of comparison. The present results are similar to the CC cases at a comparable Reynolds number

DOI: 10.1002/fld

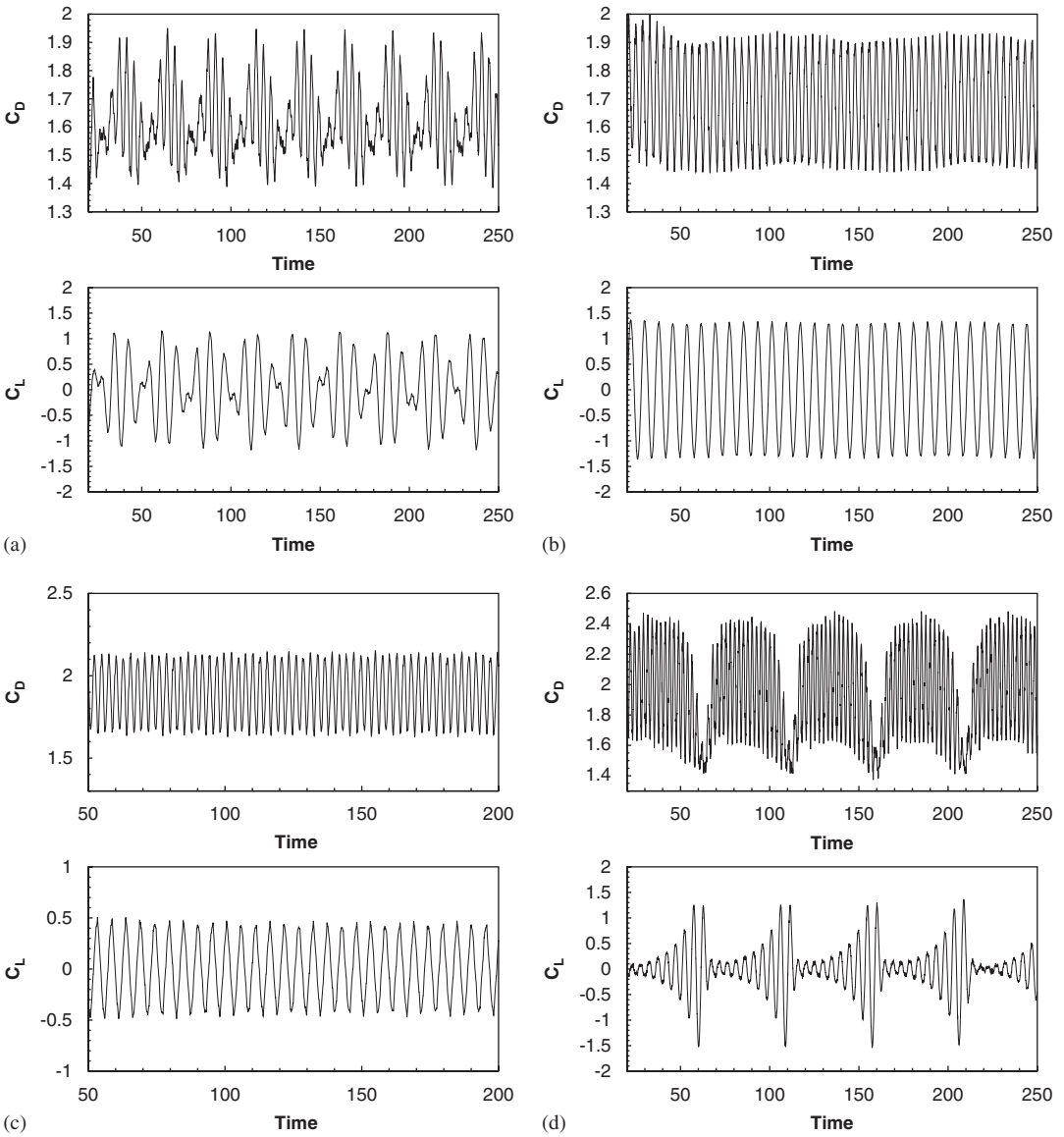

Figure 13. Time traces of drag and lift coefficients at $Re = 150$: (a) $f_r = 0.7$; (b) $f_r = 0.8$; (c) $f_r = 1.2$; and (d) $f_r = 1.3$.

and amplitude of oscillation. However, differences in $\langle C_D \rangle$ outside the synchronization band are observed. Moreover, the boundaries of the 'lock-on' regime are marginally different compared with the CC flow at a comparable Reynolds number.

The reduction in the thickness of the shear layers with an increase in f_r, as seen in Figure 11, causes greater shear forces on the horizontal faces of the cylinder owing to larger velocity gradient.

DOI: 10.1002/fld

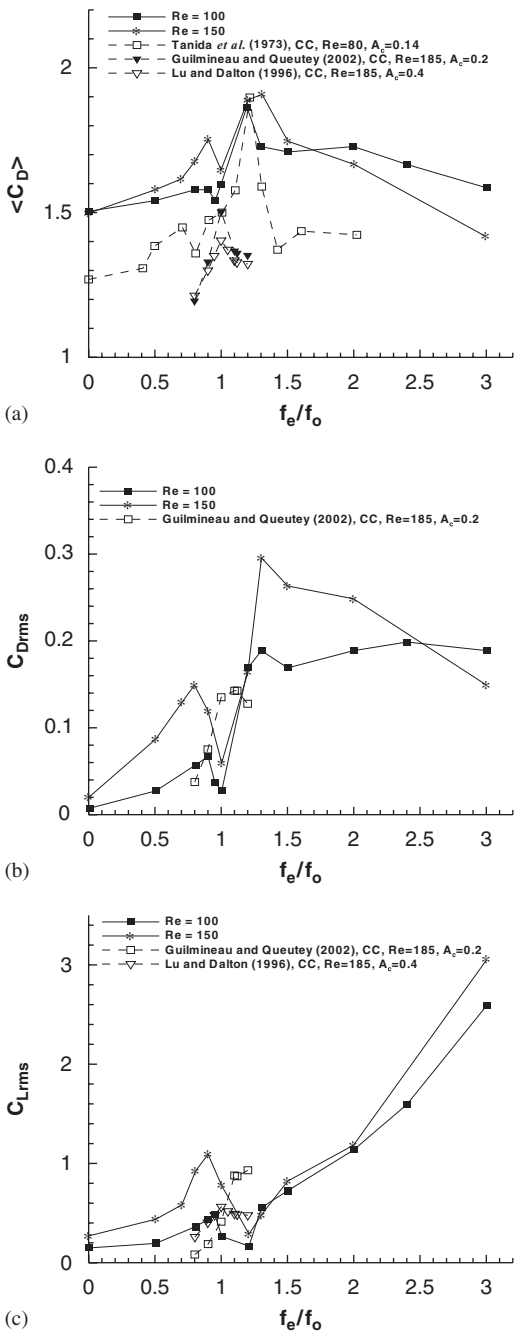

Figure 14. Variation of time averaged force coefficients with frequency ratios: (a) mean drag; (b) root mean square of drag coefficient; and (c) root mean square of lift coefficient.

DOI: 10.1002/fld

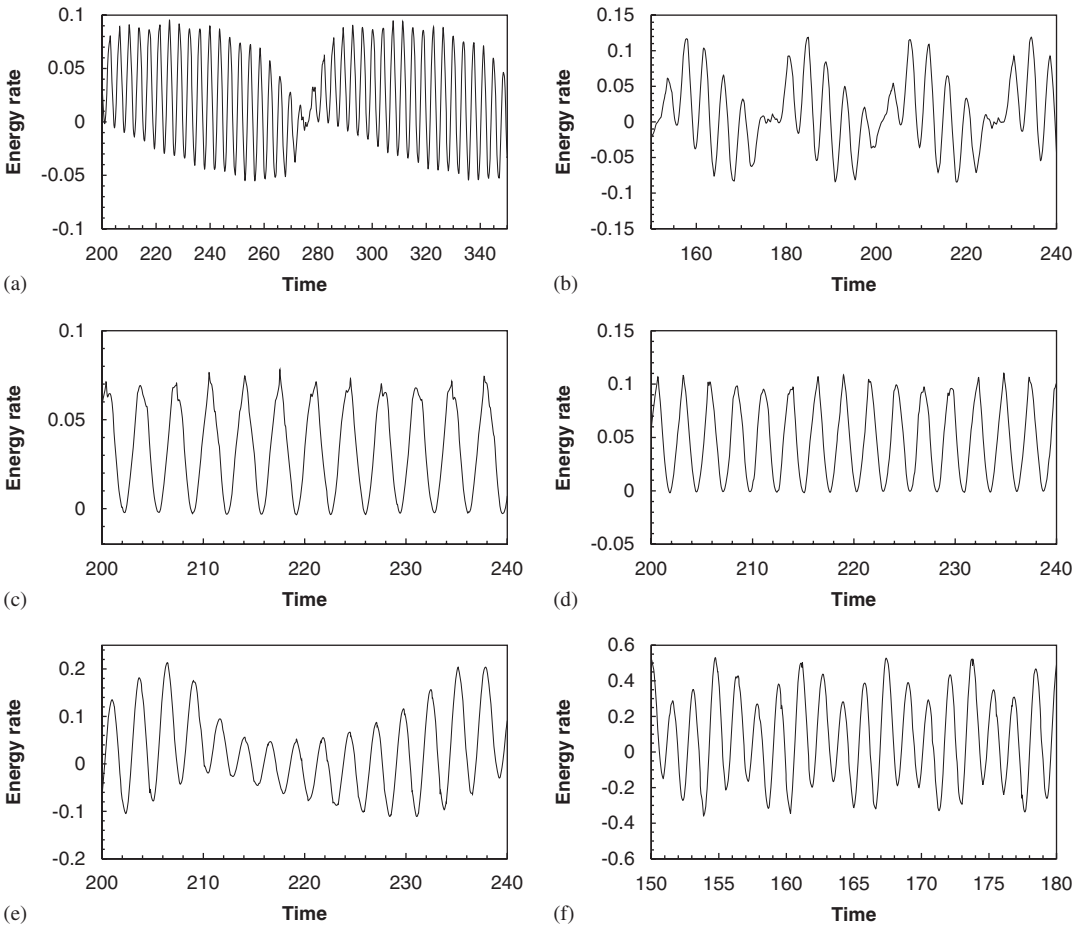

Figure 15. Temporal variation of the energy rate: (a) $f_r = 0.9,\ Re = 100$; (b) $f_r = 0.7,\ Re = 150$; (c) $f_r = 1.0,\ Re = 100$; (d) $f_r = 1.2,\ Re = 150$; (e) $f_r = 1.3,\ Re = 100$; and (f) $f_r = 2.0,\ Re = 150$.

Moreover, due to widening of the downstream wake, the pressure drag also increases. Thus, both the drag coefficient and its fluctuating part increases as the flow approaches the synchronization band. However, in the 'lock-in' regime, a single-frequency oscillation of the wake organizes the flow, causing a dip in the fluctuating part of the drag coefficient. With further increase in f_r, twin frequencies reappear in the near wake with a moderate-to-highly chaotic state, which results in greater values of C_D and its fluctuation. Outside the 'lock-in' regime, as the wake recovers its natural mode of oscillation, a trend toward the stationary cylinder C_D value is observed. The RMS fluctuations of the lift coefficient (C_{Lrms}) shows the same trend as that of C_{Drms} with the only exception that it monotonically increases beyond the synchronization regime. This is because at $f_r > 1.5$, the high acceleration of the cylinder leads to a higher vertical pressure oscillation across the cylinder resulting in a monotonic increase in the fluctuation level of the lift force. Comparing the time signals of the force coefficients at two Reynolds numbers, it is

DOI: 10.1002/fld

found that the amplitudes of drag and lift forces increase with the Reynolds number. This is in agreement with what was observed by Patnaik *et al.* [9] at $Re=80$ and 144 in case of an oscillating CC.

4.6. Energy transfer

Energy transfer is defined as the work done on the cylinder by the fluid. The mechanical energy transfer from the fluid to the oscillating cylinder per motion cycle can be written in non-dimensional form as

$$C_{\mathrm{E}}=\int_T C_L v\,\mathrm{d}\tau$$

where v is the cylinder transverse velocity, τ is the non-dimensional time and T is the time period of cylinder oscillation. Figure 15 shows the time signals of the non-dimensionalized energy rate ($C_L v$). In the 'lock-in' regime, energy flow is unidirectional and energy transfer over a period of oscillation remains almost constant (see Figures 15(c) and (d)) due to the existence of a single frequency and a constant phase between the cylinder (its transverse velocity v) and the wake (lift force) oscillation. Moreover, a positive energy rate, similar to the case of a CC [10], indicates energy transfer from the fluid to the cylinder through the lift force. This situation is close to the 'vortex-induced-vibration' where flow induces vibration of a bluff body by fluctuating lift force. In the asynchronous regime, the energy rate is either negative or positive with a variable amplitude. This shows the presence of a two-way coupling with energy being transferred either to the cylinder or to the fluid. As outside the synchronous band the cylinder and the wake oscillate at different frequencies, a correlation exists between the change in the sign of C_{E} with the direction of the phase between the lift and cylinder displacement [26].

The average energy transfer rate in the synchronization band is shown in Figure 16. As the lift force determines the nature of the energy transfer, the trend in the figure closely follows that of Figure 14(c) (in the synchronization band). The energy coefficient is always positive in the 'lock-in' regime. At higher Reynolds numbers, more energy is transferred from the fluid to the cylinder owing to the greater instantaneous magnitude of the lift force.

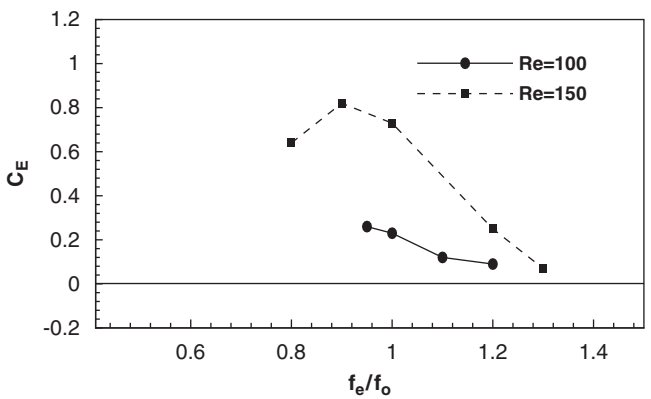

Figure 16. Energy coefficient in the 'lock-in' regime.

DOI: 10.1002/fld

5. CONCLUSIONS

A numerical study of unconfined flow past an oscillating square cylinder at $Re=100$ and 150 is carried out for the excitation frequency range $0.5f_0 \leqslant f_e \leqslant 3f_0$ (f_0 being the natural shedding frequency of the stationary cylinder) and amplitude of oscillation $0.2d$. Band limited synchronization is seen to occur at $f_r(f_e/f_0) \approx 1$ where the wake oscillates with the cylinder at the excitation frequency. The near-wake vortex shedding occurs with both the excitation and the natural frequencies being present below the 'lock-in' regime, while the forced frequency dominates at higher excitation frequencies above the synchronization period. The far wake recovers the natural mode of oscillation beyond the synchronization band resulting in the existence of multi-polar vortices at the super-harmonic state. The behavior of the near and far wake emphasizes the large-scale features of the vortex shedding from a bluff body where the wake retains its fluctuating characteristics ($f_s \approx f_0$) by adjusting a dissimilar mode locally for small departures from its usual state ($f_e \approx f_0,\ A_c/d<1$). Phase portraits of velocities in the far wake indicate the onset of a chaotic regime at higher excitation ($f_r \geqslant 3$). A vortex switch, marked by an almost 180° phase shift in the formation of shear layers, is observed at the boundaries of the 'lock-in' range. This change has a strong correlation with the sign of the mechanical energy transfer between the cylinder and the flow. Positive (flow feeds energy to the cylinder) energy transfer in the 'lock-in' range is close to the flow-induced vibration case. Thus, for asynchronous excitation, a two-way coupling (positive and negative energy transfer) between the flow and the cylinder can provide new information regarding the global nature and stability of bluff body wake at low Reynolds numbers.

REFERENCES

1. Williamson CHK. Vortex dynamics in the cylinder wake. *Annual Review of Fluid Mechanics* 1996; **28**:477–539.
2. Zdravkovich MM. Smoke observation of the formation of a Kármán vortex street. *Journal of Fluid Mechanics* 1969; **37**:491–496.
3. Ongoren A, Rockwell D. Flow structure from an oscillating cylinder, part 1. Mechanism of phase shift and recovery in the near wake. *Journal of Fluid Mechanics* 1988; **191**:197–223.
4. Bishop RED, Hassan AY. The lift and drag forces on a circular cylinder oscillating in a flowing fluid. *Proceedings of the Royal Society of London, Series A* 1964; **277**:51–75.
5. Stansby PK. The locking-on of vortex shedding due to cross-section vibration of circular cylinders in uniform and shear flows. *Journal of Fluid Mechanics* 1976; **74**:641–655.
6. Griffin OM, Hall MS. Review—vortex shedding lock-on and flow control in bluff body wakes. *Transactions of the ASME, Journal of Fluids Engineering* 1991; **113**:526–537.
7. Tanida Y, Okajima A, Watanbe Y. Stability of a circular cylinder oscillating in uniform flow or in a wake. *Journal of Fluid Mechanics* 1973; **61**:769–784.
8. Chyu C, Gu W, Rockwell D. Timing of vortex formation from an oscillating cylinder. *Physics of Fluids* 1994; **6**:3677–3682.
9. Patnaik BSV, Narayana PAA, Seetharamu KN. Numerical simulation of laminar flow past a transversely vibrating circular cylinder. *Journal of Sound and Vibration* 1999; **228**:459–475.
10. Blackburn HM, Henderson RD. A study of two-dimensional flow past an oscillating cylinder. *Journal of Fluid Mechanics* 1999; **385**:255–285.
11. Guilmineau E, Queutey P. A numerical simulation of vortex shedding from an oscillating circular cylinder. *Journal of Fluids and Structures* 2002; **16**:773–794.
12. Yang SJ, Chang TR, Fu WS. Numerical simulation of flow structures around an oscillating rectangular cylinder in a channel. *Computational Mechanics* 2005; **35**:342–351.
13. Bearman PW, Obasaju ED. An experimental study of pressure fluctuations on fixed and oscillating square-section cylinders. *Journal of Fluid Mechanics* 1982; **119**:297–321.
14. Taylor I, Vezza M. Calculations of the flow field around a square section cylinder undergoing forced oscillations using discrete vortex method. *Journal of Wind Engineering and Industrial Aerodynamics* 1999; **82**:271–291.

DOI: 10.1002/fld

15. Pope SB. *Turbulent Flows*. Cambridge University Press: Cambridge, 2000.
16. Orlanski I. A simple boundary condition for unbounded hyperbolic flows. *Journal of Computational Physics* 1976; **21**:251–269.
17. De AK, Eswaran V. A high-order accurate method for two-dimensional incompressible viscous flows. *International Journal for Numerical Methods in Fluids* 2007; **53**:1613–1628.
18. Sohankar A, Norberg C, Davidson L. Simulation of three-dimensional flow around a square cylinder at moderate Reynolds numbers. *Physics of Fluids* 1999; **11**:288–306.
19. Saha AK, Biswas G, Muralidhar K. Three-dimensional study of flow past a square cylinder at low Reynolds numbers. *International Journal of Heat and Fluid Flow* 2003; **24**:54–66.
20. Sharma A, Eswaran V. Heat and fluid flow across a square cylinder in the two dimensional laminar flow regime. *Numerical Heat Transfer*, *Part A* 2004; **45**(3):247–269.
21. Sohankar A, Norberg C, Davidson L. Low-Reynolds-number flow around a square cylinder at incidence: study of blockage, onset of vortex shedding and outlet boundary condition. *International Journal for Numerical Methods in Fluids* 1998; **26**:39–56.
22. De AK, Dalal A. Numerical simulation of unconfined flow past a triangular cylinder. *International Journal for Numerical Methods in Fluids* 2006; **52**:801–821.
23. Obasaju ED, Bearman PW, Graham JM. A study of forces, circulation and vortex patterns around a circular cylinder in oscillating flow. *Journal of Fluid Mechanics* 1988; **196**:467–494.
24. Williamson CHK, Roshko A. Vortex formation in the wake of an oscillating cylinder. *Journal of Fluids and Structures* 1988; **2**:355–381.
25. Ongoren A, Rockwell D. Flow structure from an oscillating cylinder, part 2. Mode competition in the near wake. *Journal of Fluid Mechanics* 1988; **191**:225–245.
26. Leontini JS, Stewart BE, Thompson MC, Hourigan K. Wake state and energy transition of an oscillating cylinder at low Reynolds number. *Physics of Fluids* 2006; **18**:067101.

DOI: 10.1002/fld